

Deep learning-based prediction of Precipitable Water Vapor in the Chajnantor area

Alison Matus-Bello^{1,2,3,4}, Silvia E. Restrepo^{5,6}, Ricardo Bustos⁵, Yi Hu⁷, Fujia Du^{8,9}, Jaime Cariñe⁵, Pablo García^{10,11}, Rodrigo Reeves¹², and Zhaohui Shang⁷

¹ Facultad de Ingeniería, Universidad Católica de la Santísima Concepción, Alonso de Ribera 2850, Concepción, Chile
e-mail: amatus@doctoradoia.cl

² Departamento Ingeniería Informática y Ciencias de la Computación, Universidad de Concepción, Concepción 4070409, Chile

³ Facultad de Ingeniería, Universidad del Bío-Bío, Collao 1202, Concepción, Chile

⁴ Departamento de Electrónica e Informática, Universidad Técnica Federico Santa María - Sede Concepción, Arteaga Alemparte 943, Concepción, Chile

⁵ Departamento de Ingeniería Eléctrica, Universidad Católica de la Santísima Concepción, Alonso de Ribera 2850, Concepción, Chile

⁶ Centro de Energía, Universidad Católica de la Santísima Concepción, Alonso de Ribera 2850, Concepción, Chile

⁷ National Astronomical Observatories, Chinese Academy of Sciences, Beijing, 100101, China

⁸ Nanjing Institute of Astronomical Optics & Technology, Chinese Academy of Science, Nanjing, 210042, China

⁹ CAS Key Laboratory of Astronomical Optics & Technology, Nanjing Institute of Astronomical Optics & Technology, Nanjing, 210042, China

¹⁰ Chinese Academy of Sciences South America Center for Astronomy, National Astronomical Observatories, CAS, Beijing 100101, China

¹¹ Instituto de Astronomía, Universidad Católica del Norte, Av. Angamos 0610, Antofagasta, Chile

¹² CePIA, Departamento de Astronomía, Universidad de Concepción, Casilla 160 C, Concepción, Chile

Received XXXX; accepted XXXX

ABSTRACT

Context. Astronomical observations at millimeter and submillimeter wavelengths heavily depend on the amount of Precipitable Water Vapor (PWV) in the atmosphere, directly affecting the sky transparency and degrading the quality of the signals received by radio telescopes.

Aims. Predictions of PWV at different forecasting horizons is crucial to support telescope operations, engineering planning, and observational scheduling and efficiency of radio observatories installed in the Chajnantor area in northern Chile.

Methods. We developed and validated a Long Short-Term Memory (LSTM) deep learning-based model to predict PWV at forecasting horizons of 12, 24, 36, and 48 hours using historical data from two 183 GHz radiometers and a weather station in the Chajnantor area.

Results. We find the LSTM method is able to predict PWV in the 12 and 24 hours forecasting horizons with Mean Absolute Percentage Error (MAPE) of ~22% compared to ~36% of the traditional Global Forecast System (GFS) method used by Atacama Pathfinder Experiment (APEX) and the Root Mean Square Error (RMSE) in mm are reduced by ~50%.

Conclusions. We present a first application of deep learning techniques for preliminary predictions of PWV in the Chajnantor area. The prediction performance shows significant improvements to traditional methods in 12 and 24 hours time windows. We also propose upgrades to improve our method in short (< 1 hour) and long (> 36 hours) forecasting timescales for future work.

Key words. Astronomical instrumentation, methods and techniques – Atmospheric effects – Site testing

1. Introduction

Astronomical observations at millimeter and submillimeter wavelengths heavily depend on atmospheric conditions, particularly the amount of Precipitable Water Vapor (PWV). This parameter describes the thickness of the water column, measured in millimeters (mm), that would result from collapsing all the water vapor contained in the atmospheric column along the observer's line of sight at a specific geographical location. The presence of PWV directly affects sky transparency, significantly degrading the quality of the signals received by radio telescopes and increasing the integration time required to detect faint astronomical sources (Radford, 2011). High levels of PWV can render scientific observations in certain bands impossible.

The Chajnantor area, located in the Atacama Desert in northern Chile, is recognized as one of the best sites in the world for (sub)millimeter astronomical observations due to its high altitude (~5000 meters above sea level, masl) and extreme atmospheric dryness (Bustos et al., 2014; Radford et al., 2016). This location hosts cutting-edge observatories such as ALMA, APEX, CLASS, Simons Observatory, and many others. Predicting PWV enables engineers and astronomers to optimize operations and the use of valuable telescope time by scheduling their observing frequencies under the most favorable atmospheric conditions, thus maximizing scientific return (Cortés et al., 2020). The highly variable nature of PWV at these altitudes requires reliable predictive tools. In this context, accurate monitoring and forecasting of PWV is crucial to support telescope operations, engineering planning, and observational scheduling.

Traditionally, PWV has been estimated using various methods such as Global Navigation Satellite Systems (GNSS), radiosondes, and radiometers operating at specific water vapor emission lines (e.g., 183 GHz). Radiometers can provide continuous and direct measurements of PWV, including sites at remote high-altitude locations with extreme environmental conditions (Otárola et al. 2010; Otárola et al. 2019; Valeria et al. 2024). While these methods provide valuable real-time measurements, they primarily address monitoring rather than proactive forecasting required for optimal observing scheduling.

Forecasting PWV often relies on global Numerical Weather Prediction (NWP) models, such as the Global Forecast System (GFS). While NWP models provide broad geographical coverage, they typically lack the fine-grained spatial and temporal resolution needed to accurately capture the rapid, localized variations in atmospheric moisture characteristics of high-altitude observatory sites like the Chajnantor area. This limitation significantly impacts the accuracy of short-term forecasts, critical for observation scheduling. Previous studies have shown that short-term PWV forecasts based on Geostationary Operational Environmental Satellites (GOES) and GFS data in the Chajnantor area present limited agreement with observations, obtaining errors of 33% in the 0.4–1.2 mm range (Marin et al., 2015), which is precisely the range where most submillimeter astronomical observations are scheduled due to the higher atmospheric transparency. The GFS model is currently being used by the APEX telescope (Güsten et al., 2006), which provides 5-day PWV forecasts in 6-hour step resolution.

Similar forecasting approaches using NWP models have also been successfully implemented at other major astronomical sites. For example, the Very Large Telescope (VLT) at Cerro Paranal and the Large Binocular Telescope (LBT) at Mount Graham, using the Meso-NH mesoscale atmospheric model, improves by a factor 2 the European Centre for Medium-Range Weather Forecasts (ECMWF) (Turchi et al., 2019). Likewise, the Weather Research and Forecasting (WRF) model has been validated at Observatorio del Roque de los Muchachos (Giordano et al., 2013) and at APEX in the Chajnantor Plateau (Pozo et al., 2016), demonstrating the widespread adoption of NWP tools in the astronomical community for PWV predictions.

In response to the inherent limitations of traditional techniques and the insufficient resolution of NWP models for site-specific forecasting, alternative and advanced data-driven approaches have emerged as powerful predictive tools. In particular, deep learning models have shown the ability to capture non-linear dependencies and temporal patterns in complex atmospheric datasets. Among these, Long Short-Term Memory (LSTM) networks stand out for their capacity to handle sequential data and forecast variables with high accuracy. Recent applications in atmospheric science report that such models often outperform traditional statistical and physical methods when trained with local, high-resolution data (Xiao et al., 2022; Hou et al., 2023; Yan et al., 2024).

In this context, the objective of the present study is to preliminarily develop and validate a deep learning-based model to predict PWV on 12, 24, 36 and 48 hours forecasting horizons using one year of radiometers and meteorological data for the Chajnantor area. In Section 2, we present the data and methodology. Section 3 describes the LSTM model. Section 4 presents the results obtained and Section 5 presents our conclusions and proposed future work.

2. Data and Methodology

In this study, data from 183 GHz radiometers and meteorological records from the Chajnantor area were used to develop a deep learning-based model capable of predicting PWV values. The methodology includes data collection, preprocessing, and modeling, as detailed below:

2.1. 183 GHz Radiometer Data

We used PWV data collected by two 183 GHz radiometers sensitive to the water vapor emission line in the atmosphere at this frequency. One radiometer was installed in Llano de Chajnantor at the Atacama Pathfinder Experiment (APEX) telescope site, located at coordinates 23° 00' 20.8" S, 67° 45' 33.0" W, at an altitude of 5,105 masl. The second radiometer is operated by the Universidad Católica de la Santísima Concepción (UCSC) in collaboration with the Universidad de Concepción (UdeC) and is located on Cerro Toco at the CLASS radio telescope site at 22° 57' 34.6" S, 67° 47' 13.8" W, at 5,200 masl. The horizontal distance between both sites is approximately 5.9 km.

Both instruments provide continuous high time-resolution data. PWV from APEX (APEX PWV) is available at one-minute average intervals while PWV from the UdeC-UCSC radiometer (PWV UCSC) is available every 2-second sampling intervals and then averaged to match the same 1-minute intervals.

The selected datasets for both instruments spans from July 13, 2023 to October 14, 2024 (460 days) to capture at least one annual cycle.

2.2. Meteorological Data

The meteorological data used in this study were obtained from the automated weather station located at the APEX telescope site. This station provides continuous monitoring of local atmospheric conditions such as relative humidity (RH) in percentage, temperature (Temp) in degrees Celsius, wind speed (WS) in meters per second, and wind direction (WD) in degrees.

The dataset spans from July 13, 2023, to October 14, 2024, matching the radiometer data, and serves as the basis for this preliminary investigation into PWV forecasting at this site. With a sampling interval of 1-minute, the dataset comprises approximately 662,400 records per variable. This temporal resolution enables to capture both short-term fluctuations (such as diurnal cycles and rapid weather changes) and annual seasonal patterns.

Meteorological data, PWV measurements, and GFS forecast data collected at APEX are publicly available through the APEX website: <http://www.apex-telescope.org>.

2.3. Data Preprocessing

To ensure the reliability of the predictive model, a preprocessing workflow was applied to the raw dataset. The workflow involved several sequential steps applied to the initial 1-minute resolution data: 1) data cleaning and outlier removal; 2) linear interpolation to fill missing values; 3) temporal averaging to 3-hour intervals; 4) datasets selection of meteorological variables; 5) Fourier analysis; 6) wavelet-based denoising filter; and 7) z-score normalization of all features.

2.3.1. Data Cleaning

The process began with data cleaning, where outliers were identified and removed using the Interquartile Range (IQR) method.

Specifically, any data points falling below the first quartile minus 1.5 times the IQR or above the third quartile plus 1.5 times the IQR were considered outliers.

2.3.2. Imputation of Missing Values

The dataset used in this study, composed of PWV UCSC, PWV APEX, Temp, RH, WS, and WD contained missing data in several variables. PWV UCSC had 0.22% of missing values while PWV APEX had 10.9%. Temp, HR, WS, and WD recorded at APEX each had 7.8% missing entries. These gaps were distributed throughout the year and likely resulted from instrumental issues, such as sensor saturation, temporary outages, or data logging interruptions.

To ensure continuity in the time series, missing values were imputed using linear interpolation. This method was selected for its simplicity and its effectiveness in estimating short, isolated gaps—typically under 30 minutes—without introducing artificial trends or discontinuities.

Furthermore, since the data were subsequently averaged into 3-hour intervals, the interpolation had minimal influence on the overall signal structure. This approach helped to preserve temporal consistency across variables and ensured that the LSTM model received complete, synchronized input sequences.

2.3.3. Temporal Averaging

To reduce sensitivity to high-frequency noise and short-term variability, all time series were averaged into 3-hour intervals. This resolution facilitates the identification of broader atmospheric trends relevant to medium-range PWV forecasting (12 to 48 hours), while also helping to reduce the dimensionality of the input data.

Additionally, the 3-hour interval aligns with the temporal resolution of operational forecasting models such as GFS, supporting future comparative analysis and potential integration. All variables were resampled and synchronized on the same temporal basis to ensure consistency between inputs.

2.3.4. Correlation and Input Parameters Selection

A Pearson correlation analysis was performed to guide the variable selection process, retaining only those with a statistically significant relationship to the target variable, PWV APEX. The Pearson correlation coefficient r is defined as:

$$r = \frac{\sum_{i=1}^n [(x_i - \bar{x})(y_i - \bar{y})]}{\sqrt{\sum_{i=1}^n (x_i - \bar{x})^2 \sum_{i=1}^n (y_i - \bar{y})^2}} \quad (1)$$

Where x_i and y_i are the samples of each variable, \bar{x} is the mean of the x values, \bar{y} is the mean of the y values, and n is the total number of observations. PWV APEX corresponds to y .

The analysis seen in Figure 1 revealed an expected strong positive correlation between PWV APEX and PWV UCSC ($r = 0.94$), and moderate correlations with RH ($r = 0.45$) and Temp ($r = 0.43$). In contrast, WS and the U and V wind components showed negligible correlations (all $|r| < 0.20$) and were excluded from the model due to their limited predictive value. As a result, the selected input variables are: 1) PWV APEX, 2) PWV UCSC, 3) Temp, and 4) RH.

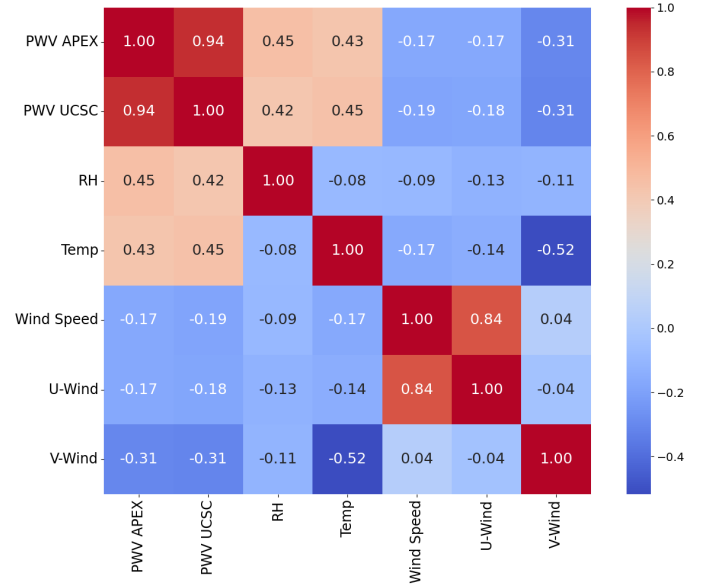


Fig. 1: Correlation matrix showing the relationships between PWV APEX, PWV UCSC, relative humidity (RH), temperature (Temp), wind speed (WS), and wind components (U and V). Warmer colors indicate positive correlations, while cooler colors indicate negative correlations.

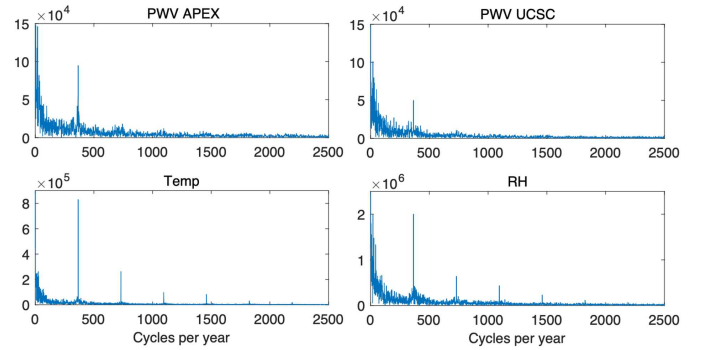


Fig. 2: Power spectral density plots from the FFT analysis of PWV APEX, PWV UCSC, Temp, and RH. The x-axis represents frequency in cycles per year.

2.3.5. Fourier Analysis

To better understand the dominant periodicities and its cyclic behavior in PWV and meteorological variables, a Fast Fourier Transform (FFT) was applied. The FFT obtained for each variable is seen in Figure 2, revealing clear peaks at frequencies corresponding to a yearly cycle (1 per year), daily cycles (365 cycles per year), and sub-daily harmonics, indicating that these signals contain predictable recurring patterns. These insights supported the decision to use sequential models such as LSTM, which are capable of capturing temporal dependencies.

2.3.6. Wavelet Denoising Filter

To improve the signal-to-noise ratio, a wavelet-based denoising technique was applied using the Symlet 4 (Sym4) wavelet function. This wavelet was selected after testing alternatives such as Daubechies 4 (db4), Coiflet 4 (coif4), and Haar, offering the best

balance between noise reduction and preservation of key signal trends.

In this context, noise in the PWV data primarily stems from instrumental fluctuations and abrupt environmental changes, which introduce high-frequency variations that can obscure relevant temporal patterns. These distortions reduce the model's ability to learn consistent relationships.

The wavelet filter effectively suppresses high-frequency noise while retaining low-frequency components crucial for trend analysis. As a result, the smoothed signals exhibit reduced short-term variability and improve model training stability and accuracy.

2.3.7. Data Normalization

All selected input variables were normalized using z-score standardization (zero mean and unit variance). This step ensures that differences in magnitude among variables do not bias the model training process and allows the LSTM network to converge more efficiently. With all variables normalized and the input structure defined, the four selected datasets at 3-hour intervals were prepared for training and evaluation using the deep learning model.

3. Deep Learning model: LSTM

In this study, a deep learning model based on recurrent neural networks, specifically Long Short-Term Memory (LSTM), was developed for the prediction of PWV. These networks are particularly suitable for sequential data analysis due to their ability to handle both short- and long-term temporal relationships. This is made possible by their memory cell-based architecture, which surpasses the limitations of traditional recurrent networks, such as gradient vanishing or explosion (Hochreiter & Schmidhuber, 1997; Hou et al., 2023; Haputhanthri & Wijayasiri, 2021; Jain et al., 2020).

The model uses as input the selected predictors (PWV UCSC, Temp, HR), together with historical values of the target variable (PWV APEX), to forecast future PWV APEX values. To ensure the integrity of the predictive process and avoid biases known as “data leakage”, only past values were used as inputs and targets, replicating realistic forecasting conditions.

The network was configured to analyze temporal windows of 48 steps, equivalent to 6 days of data. The architecture includes two hidden layers of 120 neurons each. This configuration was selected after conducting multiple tests, where different hidden layer sizes were compared. The final setup was chosen based on the best performance in terms of lowest root mean square error (RMSE) and highest coefficient of determination (R^2) across the 12 and 24 hours forecasting horizons.

The Adam optimizer was employed for its ability to dynamically adjust the learning rate, which improves model convergence (Yang & Wang, 2022). This provided the best balance between convergence speed and performance compared to other optimizers such as AdamW, Stochastic Gradient Descent (SGD), and RMSprop. The mean squared error (MSE) was employed as the loss function.

Figure 3 presents the architecture of the proposed LSTM model. The model takes as input four variables (Features): PWV APEX (1), PWV UCSC (2), Temp (3), and HR (4) recorded over 48 time-steps. The output consists of predicted values of future PWV APEX at four distinct time horizons: 4, 8, 12, and 16 time-steps ahead, which correspond to 12, 24, 36, and 48 hours into the future, respectively (multi-output).

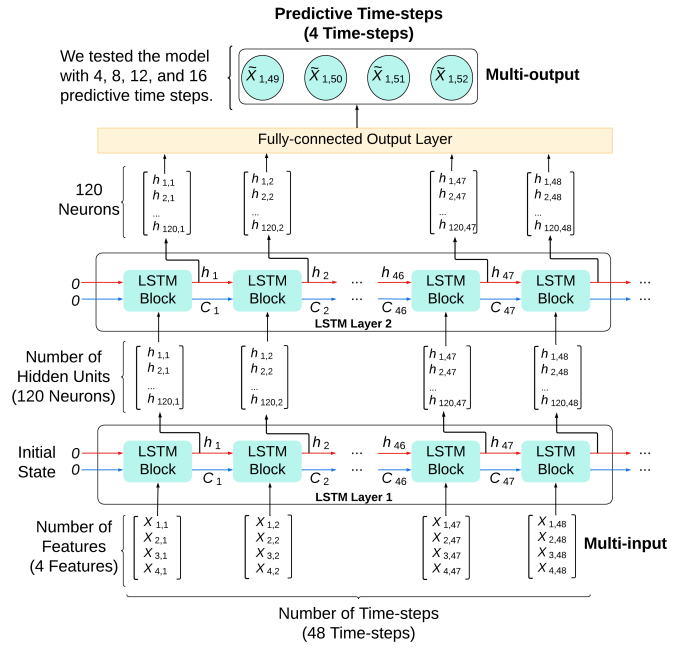


Fig. 3: Diagram of the LSTM architecture.

The architecture includes two stacked LSTM layers, each with 120 hidden units (neurons), which process the input sequence to extract relevant temporal patterns. These are followed by a fully connected output layer that maps the final LSTM outputs to the predicted values. This configuration was selected for its ability to effectively capture complex temporal dynamics while maintaining efficient training performance.

3.1. LSTM Architecture

The Long Short-Term Memory network is a type of recurrent neural network (RNN) designed to address the limitations of standard RNNs when modeling long sequences. It incorporates a memory cell regulated by three gates—input, forget, and output—that control the flow of information over time. These gates determine which information is retained, discarded, or passed to the next time step. The following formulation is adapted from standard LSTM definitions, using the approach by Hou et al., 2023. At each time step t , the gates are calculated as follows:

$$i_t = \sigma(W_i \cdot [h_{t-1}, x_t] + b_i) \quad (2)$$

$$f_t = \sigma(W_f \cdot [h_{t-1}, x_t] + b_f) \quad (3)$$

$$o_t = \sigma(W_o \cdot [h_{t-1}, x_t] + b_o) \quad (4)$$

In these expressions, x_t is the input vector at time step t , and h_{t-1} is the hidden state from the previous time step. The weight matrices W_i , W_f , W_o and bias vectors b_i , b_f , b_o are learned during training. The sigmoid activation function σ constrains the gate outputs to values between 0 and 1, effectively controlling how much information passes through each gate. The candidate cell state \tilde{C}_t , which represents new information to be considered for memory update, is computed as:

$$\tilde{C}_t = \tanh(W_c \cdot [h_{t-1}, x_t] + b_c) \quad (5)$$

Here, W_c and b_c are the weight matrix and bias associated with the candidate state, and \tanh is the hyperbolic tangent ac-

tivation function. The cell state C_t is updated by combining the previous state with the candidate state, modulated by the forget and input gates, respectively:

$$C_t = f_t \odot C_{t-1} + i_t \odot \tilde{C}_t \quad (6)$$

The symbol \odot denotes the Hadamard (element-wise) product, allowing for selective control over each element of the state vector. Finally, the hidden state h_t , which also serves as the output of the LSTM cell, is computed using the output gate and the updated cell state:

$$h_t = o_t \odot \tanh(C_t) \quad (7)$$

This mechanism enables the LSTM network to maintain long-term dependencies in sequential data, while adaptively filtering relevant information at each time step.

3.2. LSTM Model Implementation

The model was implemented in MATLAB R2024b and Python 3.8.20 for cross-validation. The dataset was split into training (80%) and validation (20%). The training data covered the period from July 13, 2023, to July 14, 2024, while the validation data ranged from July 15, 2024, to October 14, 2024. Training was conducted over 180 epochs using the Adam optimizer.

3.3. LSTM Model Evaluation

The model's performance was evaluated using multiple metrics, including the correlation coefficient (r), coefficient of determination (R^2), root mean squared error (RMSE), mean absolute error (MAE), and mean absolute percentage error (MAPE).

R^2 measures the proportion of variability in the actual data explained by the model. Values close to 1 indicate an excellent fit. R^2 is defined as:

$$R^2 = 1 - \frac{\sum_{i=1}^n (\hat{y}_i - \bar{y})^2}{\sum_{i=1}^n (y_i - \bar{y})^2} \quad (8)$$

Where y_i denotes the observed (true) values, \hat{y}_i is the predicted value for each i , \bar{y} is the mean of the observed values, and n is the total number of observations.

The RMSE was also employed to measure the average magnitude of errors between predictions and actual values, giving greater weight to larger errors. Its interpretation is intuitive, as it is expressed in the same units as the target variable in mm.

$$\text{RMSE} = \sqrt{\frac{1}{n} \sum_{i=1}^n (y_i - \hat{y}_i)^2} \quad (9)$$

Additionally, the MAE was used as a complementary metric, representing the average absolute difference between predicted and actual values. Unlike RMSE, MAE treats all errors equally without emphasizing larger deviations, making it useful for assessing overall prediction performance.

$$\text{MAE} = \frac{1}{n} \sum_{i=1}^n |y_i - \hat{y}_i| \quad (10)$$

Finally, the MAPE was calculated to express the average error as a percentage relative to the actual values. This metric is particularly useful for evaluating model performance across different scales, although it may be less stable when actual values approach zero.

$$\text{MAPE} = \frac{1}{n} \sum_{i=1}^n \left| \frac{y_i - \hat{y}_i}{y_i} \right| \times 100\% \quad (11)$$

To further assess the model's performance, we generated a set of plots, including the evolution of loss during training, predicted versus actual value comparisons, and scatter plots with regression lines.

4. Results and Discussion

This section presents the results obtained from LSTM predictions of PWV APEX compared with real future values of PWV measured at APEX. The performance was evaluated for different forecasting of 4-8-12-16 steps, corresponding to forecasting horizons of 12-24-36-48 hours.

4.1. Comparative Evaluation for Different Forecasting Horizons

Table 1 presents the performance of the LSTM model across the four forecasting horizons. The results show a strong correlation r and high R^2 for short-term predictions (12 and 24 hours) of real PWV values. In these forecasting horizons, RMSE is ~ 0.35 mm, MAE ~ 0.24 mm, and MAPE $\sim 22\%$.

The prediction accuracy decreases as the forecasting horizon increases. The RMSE increases steadily from 0.328 mm (12h) to 0.916 (48h) mm. An RMSE approaching 1 mm signifies a considerably larger uncertainty in atmospheric conditions, potentially impacting the feasibility or quality of PWV predictions. The MAPE also increases with the forecasting horizon, rising from 21.1% (12h) to 65.9% (48h). Notably, there is a sharp increase in MAPE between the 24h forecast (23.2%) and the 36h forecast (62.8%). While the absolute errors (RMSE, MAE) show a more gradual increase, this jump in MAPE highlights that the relative prediction error, in agreement with RMSE results, becomes particularly significant at 36 hours.

This indicates that LSTM model can predict a significant portion of the observed PWV in short timeframes (12 and 24 hours), suggesting the utility of the predictions for operational tasks sensitive to PWV conditions. The ability to predict PWV diminishes considerably at longer horizon times, potentially limiting its quantitative use for forecasts beyond one and a half day.

4.2. Scatter Analysis of Predicted vs Real PWV

Figure 4 presents scatter plots of the predicted versus real PWV values for each forecasting horizon, including the regression line. The tight clustering of data points along the regression line for the 12 and 24 hours horizons visually reinforces the strong correlation and higher accuracy metrics reported. However, as the forecasting horizon increases to 36 and 48 hours, the scatter increases significantly, and the values of r and R^2 drop substantially, indicating a weaker linear relationship and reduced predictive power, consistent with the quantitative metrics.

Table 1: Performance of the LSTM model for different forecasting horizons

Steps	Time	r	R^2	RMSE (mm)	MAE (mm)	MAPE (%)
4	12h	0.9492	0.9009	0.328	0.230	21.1
8	24h	0.9336	0.8704	0.376	0.256	23.2
12	36h	0.6917	0.4583	0.768	0.547	62.8
16	48h	0.5578	0.2297	0.916	0.614	65.9

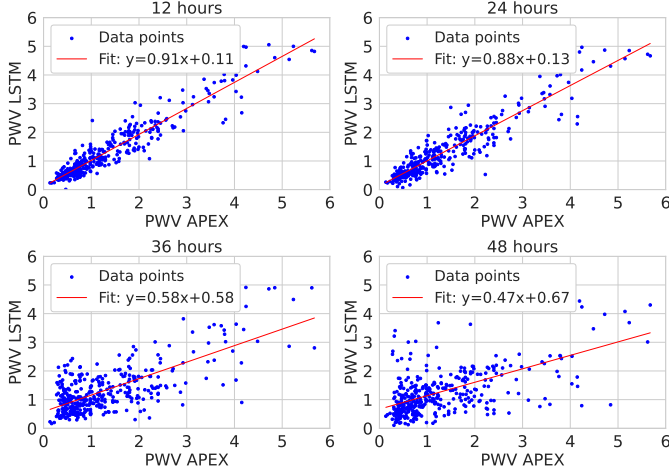


Fig. 4: Scatter plots comparing PWV LSTM with PWV APEX at the four different forecasting horizons. Each subplot includes a linear regression fit line.

4.3. Temporal Comparison Between Predicted and Real PWV

Figure 5 illustrates the temporal comparison between the predicted values by the LSTM model (PWV LSTM) and the real observed values recorded by APEX (PWV APEX) across the four forecast horizons. The plots visually confirm that the model effectively captures the temporal dynamics and amplitude variations of PWV over time, particularly for the short-term forecasts (12 and 24 hours) where the predicted series closely tracks the observations. A greater divergence between the predicted and real PWV series is observed at longer horizons (36 and 48 hours), consistent with the increasing error metrics (r , R^2 , RMSE, and MAE) and the sharp rise in MAPE previously noted.

4.4. Performance Comparison Between LSTM and GFS

We analyzed the LSTM and GFS prediction results in the same period of time, same time-resolution, and same forecasting horizons for a direct comparison between these models. The GFS data (PWV GFS) are the predictions obtained at APEX with a total of 5-day forecasting horizon in steps of 6-hour resolution. We only considered the 12, 24, 36, and 48 hours forecasting horizons to match with our LSTM predictions. Figure 6 compares these predictions with PWV APEX at each forecasting horizon. The differences between the LSTM and GFS models with real values (PWV LSTM – PWV APEX and PWV GFS – PWV APEX) are shown in Figure 7.

Confirming the results shown in Figure 6, the LSTM model is able to reduce the RMSE in short-term forecasts (12 and 24 hours), achieving a $RMS E_{LSTM}$ of 0.328 and 0.376 mm, respectively. These are notably lower than $RMS E_{GFS}$ of 0.625 and 0.636 mm, reducing the error by ~50%. Analyzing MAPE val-

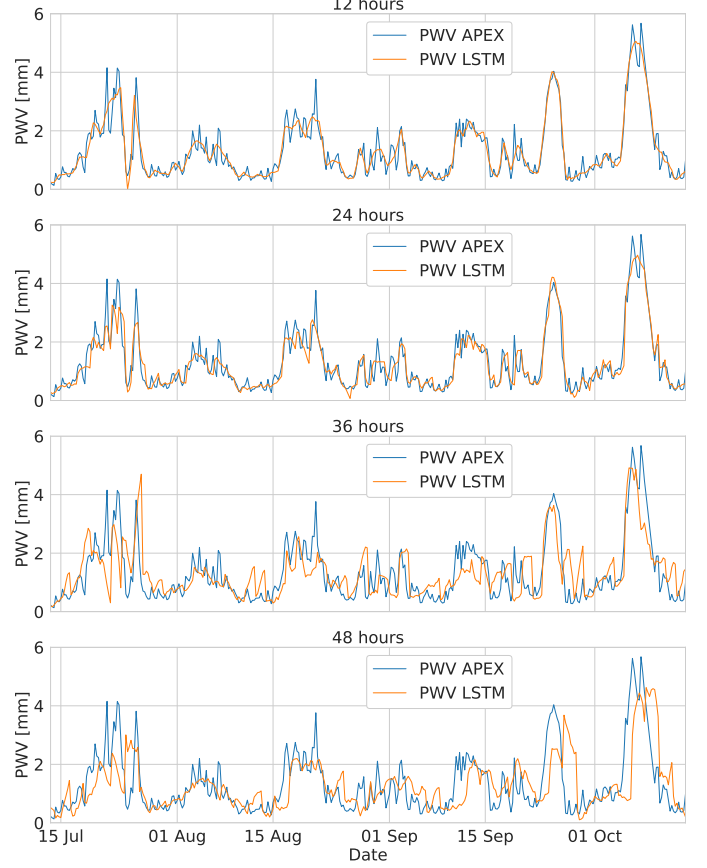


Fig. 5: Comparison between PWV APEX (blue) and PWV LSTM (orange) for different forecasting horizons. PWV LSTM closely tracks the temporal dynamics of PWV APEX, particularly in 12 and 24 hours predictions.

ues, we find the overall error for LSTM to be within ~22% while for GFS are within ~36%, as seen in Table 2.

Table 2: Comparison of $RMSE$ (mm) and $MAPE$ (%) between LSTM and GFS differences with PWV APEX.

Time	$RMS E_{LSTM}$	$RMS E_{GFS}$	$MAPE_{LSTM}$	$MAPE_{GFS}$
12h	0.328	0.625	21.1	35.6
24h	0.376	0.636	23.2	36.2
36h	0.768	0.662	62.8	36.8
48h	0.916	0.644	65.9	36.0

For 36 and 48 hours horizons, $RMS E_{LSTM}$ increases to 0.768 and 0.916 mm, surpassing the GFS model with $RMS E_{GFS}$ of 0.662 and 0.644 mm.

At high PWV values, the differences between LSTM and GFS with APEX become higher. To analyze in the same PWV

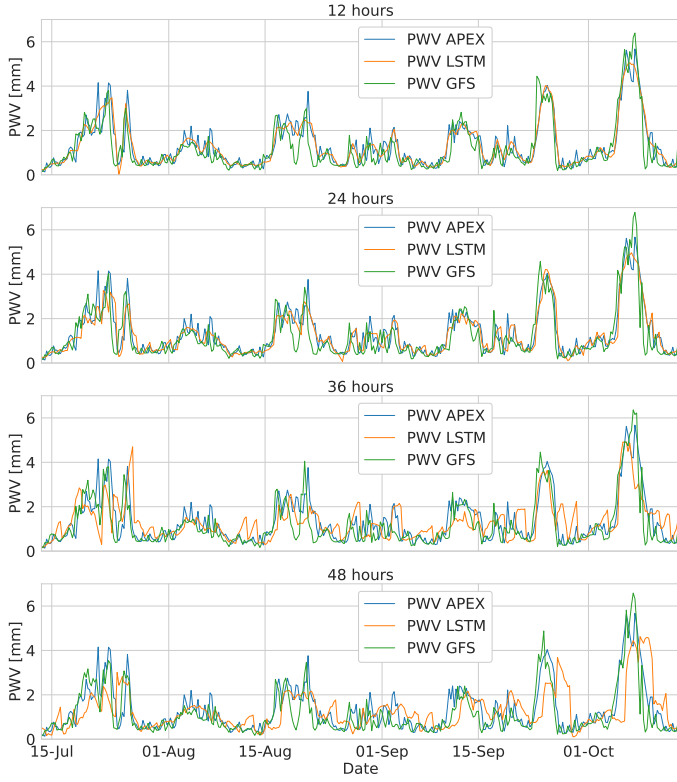


Fig. 6: Comparison between PWV LSTM (orange), PWV GFS (green), and PWV APEX (blue). Each subplot corresponds to different forecasting horizons.

range (0.4–1.2 mm) studied in Marin et al., 2015, we obtained the following comparison between LSTM and GFS in Table 3.

Table 3: Comparison of RMSE (mm) and MAPE (%) between LSTM and GFS differences with PWV APEX in the 0.4–1.2 mm range.

Time	$RMSE_{LSTM}$	$RMSE_{GFS}$	$MAPE_{LSTM}$	$MAPE_{GFS}$
12h	0.235	0.356	23.2	35.9
24h	0.245	0.385	25.1	36.3
36h	0.631	0.393	67.9	36.1
48h	0.595	0.362	63.3	34.4

In the 0.4–1.2 mm range, for 12 and 24 hours forecasting horizons, $RMSE_{LSTM}$ is ~ 0.24 mm and $RMSE_{GFS} \sim 0.36$ mm, presenting a reduction of $\sim 33\%$ for LSTM compared with GFS. $RMSE_{LSTM}$ increases for longer forecasting horizons at 36 and 48 hours. MAPE results present similar percentage values to those found for all PWV data range.

5. Conclusions and Future Work

This study presents a first investigation into the application of deep learning techniques (specifically LSTM networks) for preliminary predictions of PWV in the Chajnantor area. Using high time-resolution radiometric and meteorological data collected locally for more than 1 year, a site-specific LSTM-based forecasting model was developed and evaluated.

The LSTM model demonstrated higher predictive accuracy for 12 and 24 hours forecasting horizons, where it outperformed the traditional GFS method in r , R^2 , RMSE, MAE, and MAPE



Fig. 7: Differences of PWV LSTM (orange) and PWV GFS (green) with PWV APEX. Each subplot corresponds to different forecasting horizons.

metrics, reducing the prediction errors by $\sim 50\%$. However, the LSTM model performance declined beyond the 36 and 48 hours horizon, with an increase in error variability and relative error. This degradation, while expected in time series forecasting, suggests that further improvements are needed before the model can reliably support longer-term astronomical observing planning.

These results highlight the potential of deep learning as a valuable tool for short-term operational PWV forecasting at high-altitude observatory sites. The ability to produce localized high-resolution forecasts tailored to specific atmospheric conditions is particularly advantageous in environments where global numerical weather models struggle to capture fine-scale moisture variability.

Future upgrades are suggested to improve our PWV predictions in very short (< 12 hours) and long (> 36 hours) timescales, focusing on several key areas: 1) expand the dataset to include multiple years of historical observations to enhance model generalization and stability; 2) incorporate different variables and datasets that are correlated with PWV, including historical meteorological reanalysis data, satellite data, solar radiation, cloudiness, air pressure, and others that are available in the Chajnantor area; 3) explore different time-resolution forecast scales, for example 10 minutes or 1 hour, and larger forecasting horizons up to 1 week or more; 4) test alternative deep learning architectures such as attention-based models and Temporal Convolutional Networks (TCNs); and 5) assess real-time operational deployment potential in coordination with observatories scheduling systems. Considering these upgrades, a prospective plan

would be to produce real-time predictions at different forecasting horizons available on a public webpage.

Although this study is site-specific, the proposed methodology can be generalized to other astronomical observatory locations. To do so, it is essential to ensure the availability of high-quality, high-resolution local PWV and meteorological data for model training. Furthermore, the input variables and preprocessing steps may need to be adapted to the specific atmospheric characteristics of the new site. With sufficient data and careful retraining, the LSTM-based approach demonstrated here can be transferred to different geographic regions and used as a flexible forecasting tool for PWV predictions to support astronomical operations.

Acknowledgements. We acknowledge support from FIC-R IA 40036152-0, Gobierno Regional del Bio-Bío. We acknowledge support from China Chile Joint Research Fund CCJRF1803 and CCJRF2101. SR acknowledges support from ANID FONDECYT Iniciación 11221231. RB and SR acknowledge support from ANID FONDECYT Regular 1251819. JC acknowledges support from ANID FONDECYT Regular 1240843. We also acknowledge the availability of meteorological data, PWV, and GFS forecasts provided by the APEX telescope website.

References

- Bustos, R., Rubio, M., Otárola, A., & Nagar, N. 2014, *PASP*, 126, 1126, <https://doi.org/10.1086/679330>
- Cortés, F., Cortés, K., Reeves, R., Bustos, R., & Radford, S. 2020, *A&A*, 640, A126, <https://doi.org/10.1051/0004-6361/202037784>
- Giordano, C., Vernin, J., Vázquez Ramió, H., Muñoz-Tuñón, C., Varela, A. M., & Trinquet, H. 2013, *MNRAS*, 430, 3102, <https://doi.org/10.1093/mnras/stt117>
- Güsten, R., Nyman, L. Å., Schilke, P., Menten, K., Cesarsky, C., & Booth, R. 2006, *A&A*, 454, L13, <https://doi.org/10.1051/0004-6361:20065420>
- Haputhanthri, D. & Wijayasiri, A. 2021, *Proceedings of the 2021 Moratuwa Engineering Research Conference (MERCon)*, 602–607, <https://doi.org/10.1109/MERCon52712.2021.9525670>
- Hochreiter, S. & Schmidhuber, J. 1997, *Neural Computation*, 9(8), 1735–1780, <https://doi.org/10.1162/neco.1997.9.8.1735>
- Hou, X., Hu, Y., Du, F., Ashley, M. C. B., Pei, C., Shang, Z., Ma, B., Wang, E., & Huang, K. 2023, *Astronomy and Computing*, 43, 100710, <https://doi.org/10.1016/j.ascom.2023.100710>
- Jain, M., Manandhar, S., Lee, Y. H., Winkler, S., & Dev, S. 2020, in *Proceedings of the 2020 IEEE USNC-CNC-URSI North American Radio Science Meeting (Joint with AP-S Symposium)*, 147–148, <https://doi.org/10.23919/USNC/URSI49741.2020.9321614>
- Marín, J. C., Pozo, D., & Curé, M. 2015, *A&A*, 573, A41, <https://doi.org/10.1051/0004-6361/201424460>
- Otárola, A., Travouillon, T., Schöck, M., Els, S., Riddle, R., Skidmore, W., Dahl, R., Naylor, D., & Querel, R. 2010, *PASP*, 122(890), 470, <https://doi.org/10.1086/651582>
- Otárola, A., De Breuck, C., Travouillon, T., Matsushita, S., Nyman, L. Å., Wooten, A., Radford, S. J. E., Sarazin, M., Kerber, F., & Pérez-Beaupuits, J. P. 2019, *PASP*, 131, 998, <https://doi.org/10.1088/1538-3873/aafb78>
- Pozo, D., Marín, J. C., Illanes, L., Curé, M., & Rabanus, D. 2016, *MNRAS*, 459, 419, <https://doi.org/10.1093/mnras/stw600>
- Radford, S. J. E. 2011, *RevMexAA*, 41, 87–90, <http://arxiv.org/abs/1107.5633>
- Radford, S., & Peterson, J. 2016, *PASP*, 128, 965, <https://doi.org/10.1088/1538-3873/128/965/075001>
- Turchi, A., Masciadri, E., Kerber, F., & Martelloni, G. 2019, *MNRAS*, 482, 206, <https://doi.org/10.1093/mnras/sty2668>
- Valeria, L., Martínez-Ledesma, M., & Reeves, R. 2024, *A&A*, 684, A186, <https://doi.org/10.1051/0004-6361/202347773>
- Xiao, X., Lv, W., Han, Y., Lu, F., & Liu, J. 2022, *Atmosphere*, 13(9), 1453, <https://doi.org/10.3390/atmos13091453>
- Yan, X., Yang, W., Li, Y., et al. 2024, *Athens J. Sci.*, 11(3), 165–180, <https://doi.org/10.30958/aj.s.11-3-2>
- Yang, M., & Wang, J. 2022, *Procedia Comput. Sci.*, 199, 18–25, <https://doi.org/10.1016/j.procs.2022.01.003>